Adsorption (2014) 20:91–107
DOI 10.1007/s10450-013-9552-1

Discrete element simulation of the dynamics of adsorbents in a radial flow reactor used for gas prepurification

Olivier Dubé · Mark Ackley · Cem Celik · Jamal Chaouki · François Bertrand

Received: 18 January 2013 / Accepted: 30 April 2013 / Published online: 17 May 2013

Abstract Radial flow reactors (RFR) are used in thermal swing adsorption (TSA) processes for gas prepurification. The aim of this work is to show the validity of the discrete element method (DEM) to simulate the effect of thermal expansion and contraction cycles occurring in such processes on the packed bed of RFR reactors. Both mono-layered and bi-layered packed beds of adsorbents are investigated. A DEM-based model of a full-scale size unit was developed, the parameters of which were calibrated by means of particle-scale experimental measurements and simple auxiliary DEM simulations. The DEM-based model used is isothermal and the thermal expansion and contraction phenomena are modelled through the displacement of the inner and outer walls of the computational domain. First, the accuracy of this model is assessed using analytical values of the static wall pressure (i.e. with no wall motion) as well as experimental measurements of the dynamic wall pressure (i.e. with wall motion) of a bi-layered bed. Next, simulation results for a few process cycles in the case of a bi-layered packed bed indicates that little mixing occurs at the interface between the two types of adsorbents. To our knowledge, this is the first time that simulation is used to investigate the behavior of the packed bed of a RFR in a TSA process. The results obtained with the proposed model show that the DEM is a valuable tool for the investigation of such slow dynamical processes, provided a careful calibration is done.

Keywords Discrete element simulation · Radial flow reactor · Packed bed · Thermal swing adsorption

O. Dubé · J. Chaouki (✉) · F. Bertrand (✉)
Department of Chemical Engineering, Ecole Polytechnique de Montréal, P.O. Box 6079, Stn. CV, Montreal, QC H3C 3A7, Canada
e-mail: jamal.chaouki@polymtl.ca

F. Bertrand
e-mail: francois.bertrand@polymtl.ca

M. Ackley · C. Celik
Praxair, Inc., 175 East Park Drive, Tonawanda, NY 14150, USA

1 Introduction

Nitrogen and oxygen are the most common and extensively used industrial gases with applications in various process industries like petrochemical, metal, food, etc. They are typically produced using a cryogenic air separation unit (ASU) in which air is cooled, liquefied and separated using a distillation process. A pre-purification unit (PPU) is needed prior to cryogenic ASU to remove air impurities and contaminants such as water, carbon dioxide, nitrous oxide, light hydrocarbons, etc. Thermal swing adsorption (TSA) is commonly used for air pre-purification and is the technology of choice prior to cryogenic distillation (Kumar and Deng 2006). In an optimized TSA PPU, a typical axial packed bed reactor is filled with layers of at least two different adsorbents. The first layer is usually made of activated alumina, to remove water from the gas feed, and the second one is commonly made of a synthetic zeolite X material (NaX type like 13X molecular sieve), to remove carbon dioxide and other minor contaminants (Ackley et al. 2012; Hidano et al. 2011; Kalbassi and Golden 1999; Kumar et al. 2002). TSA processes are normally operated on a cyclic basis (Ruthven 1984; Seader and Henley 1998). The cycle involves the basic steps of (1) pressurizing the bed with feed gas, (2) passing the pressurized feed stream through the bed of adsorbents (adsorption of contaminants), (3) depressurizing the bed, (4) passing a heated regenerating gas counter-currently to the normal feed

direction (desorption of contaminants) and (5) passing a cooling gas through the bed to bring it back to its initial thermal state. The regeneration part of the process usually adopts the thermal pulse concept wherein a heat front or wave is created and it moves forward and causes a fraction of the bed to heat up entirely to the hot regeneration temperature. The cool purge is then initiated and the effect is to begin cooling the hot portion of the bed while simultaneously carrying forward the previously stored heat into the remaining forward part of the bed to complete the desorption of contaminants. Regeneration temperatures in a TSA PPU are sufficiently high, ranging typically from 150 to 300 °C, and depend on the adsorbents used and the components to be desorbed (Hidano et al. 2011; Kalbassi and Golden 1999; Ko et al. 2002; Kumar and Dissinger 1986; Ruthven 1984).

The annular packed bed (APB), also called radial flow reactor (RFR) or radial flow fixed bed reactor (RFBR), is generally used for heterogeneous catalytic processes and gas purification systems (Heggs et al. 1994; Kareeri et al. 2006). The main advantages of RFR over traditional axial flow packed bed reactors are the lower pressure drop needed for operation, the increased flow area and the higher flow rate that can be achieved. Many studies of RFR have mainly focused on gas stream uniform distribution over the active material bed height since process efficiency as well as profitability of RFR largely depend on this aspect (Celik and Ackley 2012; Heggs et al. 1995a, b; Kareeri et al. 2006; Lobanov and Skipin 1986; Ponzi and Kaye 1979). Kareeri et al. (2006) and Lobanov and Skipin (1986) showed that low bed porosity improves flow distribution. They also insisted on proper active material loading so that tight packing of active material is maintained throughout operation.

Due to the aforementioned technical advantages of RFR, there is great benefit to use this configuration for full-scale adsorption processes. However, when RFR is used in conjunction with a thermal swing regeneration step, the reactor mechanical components (e.g. reactor vessel) contract and expand because of the substantial temperature differences between the different operating phases (Ackley et al. 2012; Libal et al. 1998). The axial and/or radial relative motions between the vessel walls and the bed of adsorbents can be the source of induced thermal loads. It can also damage the adsorbent bed by breaking the particles, creating voids, inducing particle settling and promoting mixing of layered adsorbents. All of this will inevitably affect flow uniformity as well as process efficiency.

While limited, previous RFR studies have solely focused on the gas phase. Using experiments, phenomenological numerical models or computational fluid dynamics (CFD), flow direction, configuration and distribution as well as reaction conversion and selectivity in isothermal, incompressible and steady-state conditions have been investigated. No study has explored the effect of a TSA cyclic process on the particles constituting the packed bed of a RFR. Experimental investigation of particle dynamics is extremely tedious, particularly in the case of a TSA process in a RFR. Most experimental measurement techniques, whether they are invasive (e.g. sampling technique, fiber optics) or non-invasive (e.g. tomography or velocimetry techniques), are either not readily applicable or extremely costly to implement. Also, each measurement technique provides only a limited amount of information on particle behavior.

The discrete element method (DEM) is a powerful numerical simulation technique internationally recognized and used to gain valuable insight into static or dynamic behaviour of granular materials. First introduced by Cundall and Strack (1979), the DEM consists of simulating the motion of each individual particle using Newton's second law of motion. Even if the particles are considered rigid, they are allowed to overlap so as to mimic particle deformation occurring during contact. A contact model (force–displacement law) is used to relate the contact force between the particles to their overlap. DEM has been used to study a wide variety of granular processes. To name just a few, it has been successfully used to investigate discharge of silos (Balevicius et al. 2011; Gonzalez-Montellano et al. 2011; Ketterhagen et al. 2009), pressure and shear exerted by stored materials (Goda and Ebert 2005; Masson and Martinez 2000), granular mixing and segregation inside pharmaceutical blenders (Lemieux et al. 2007; Sudah et al. 2005) or cylindrical tumblers (Rapaport 2007). DEM capability of predicting realistic granular phenomena as well as flow parameters and properties are only achievable through meticulous identification of material properties, careful selection of an appropriate contact model and, most importantly, experimental verification and/or validation of the DEM-based model used (Balevicius et al. 2011; Gonzalez-Montellano et al. 2011). Material physical properties can be evaluated by experimental measurement of a property at the particle scale or by calibration using simple auxiliary DEM simulations discriminating the effect of a specific property.

In this study, the effect of cyclic thermal expansion and contraction of the vessel of a RFR, used in a TSA process for air pre-purification, on mono- and bi-layered packed beds of adsorbents is investigated using the DEM. A simplified DEM-based model of a full-scale unit is created. The DEM model is carefully calibrated using both experimental measurements and auxiliary DEM simulations. Then, the model is assessed using a mono-layered packed bed computational domain. To complete its assessment, the model is compared against analytical and experimental data of a full-scale size unit for verification and validation. A specific wall motion cycle, representing one temperature cycle of a TSA process, was considered for the simulations. Wall pressures are investigated over the course of many

cycles. Finally, the DEM-based model is applied in a bi-layered packed bed computational domain in order to investigate adsorbent migration. The results obtained with the proposed model show the usefulness of the DEM for investigating slow dynamical processes.

2 Methodology

2.1 Discrete element method

The DEM is based on a force and momentum balance on each particle. For this study, it is written as:

$$m\frac{d^2\overrightarrow{x}}{dt^2} = m\overrightarrow{g} + \sum\left(\overrightarrow{F_n} + \overrightarrow{F_t}\right) \tag{1}$$

$$I\frac{d\overrightarrow{\omega}}{dt} = \sum\left(\overrightarrow{T} + \overrightarrow{M}\right) \tag{2}$$

where $\overrightarrow{x}$, m, I and $\overrightarrow{\omega}$ denote the position vector, mass, moment of inertia and angular velocity vector of a particle. These equations are solved using a half-step leapfrog Verlet (HSLV) integration scheme (Fraige and Langston 2004). The forces involved in this model are the gravitational force $\left(m\overrightarrow{g}\right)$ and the inter-particle contact forces decomposed into normal $\left(\overrightarrow{F_n}\right)$ and tangential components $\left(\overrightarrow{F}_t\right)$. Drag and buoyant forces are neglected due to the low density of the fluid phase (air) and cohesion forces are also neglected because of the particle sizes, which are in the order of a few millimeters. $\overrightarrow{T}$ and $\overrightarrow{M}$ are the torque and rolling friction torque. They are given by:

$$\overrightarrow{T} = \overrightarrow{r} \times \overrightarrow{F_t} \tag{3}$$

$$\overrightarrow{M} = -\mu_r\left\|\overrightarrow{F_n}\right\|\frac{\overrightarrow{\omega}}{\left\|\overrightarrow{\omega}\right\|} \tag{4}$$

where $\overrightarrow{r}$ is the vector from the center of a particle to the contact point and μ_r is the coefficient of rolling resistance and has length units. To account for the elastic (*el*) and dissipation (*dis*) forces, the normal and tangential components of the contact forces are modeled using a generalized spring-dashpot model:

$$\begin{aligned}\overrightarrow{F_n} &= \overrightarrow{F_n^{el}} + \overrightarrow{F_n^{dis}} \\ &= k_n\delta_n^{\frac{3}{2}}\overrightarrow{n} + \gamma_n\delta_n^{\frac{1}{2}}\overrightarrow{v_n}\end{aligned} \tag{5}$$

$$\begin{aligned}\overrightarrow{F_t} &= \overrightarrow{F_t^{el}} + \overrightarrow{F_t^{dis}} \\ &= k_t\overrightarrow{\delta_t} + \gamma_t\overrightarrow{v_t}\end{aligned} \tag{6}$$

where $\overrightarrow{n} = \frac{\overrightarrow{r}}{\left\|\overrightarrow{r}\right\|}$, δ_n and $\overrightarrow{\delta_t}$ are respectively the normal deformation and vector of tangential deformation, and $\overrightarrow{v_n}$ and $\overrightarrow{v_t}$ are the normal and tangential components of the relative velocities between the particles in contact. $\overrightarrow{F_n^{el}}$ is evaluated with the Hertz theory while $\overrightarrow{F_n^{dis}}$ is evaluated with the Tsuji model (Tsuji et al. 1992). The tangential deformation vector is given by:

$$\overrightarrow{\delta_t} = \min\left(\int_0^{t_c}\overrightarrow{v_t}\left(t'\right)dt', \delta_{t,\max}\frac{\overrightarrow{v_t}}{\left\|\overrightarrow{v_t}\right\|}\right) \tag{7}$$

where t_c is the contact lifetime. The maximum tangential deformation is given by:

$$\delta_{t,\max} = \mu\frac{(2-\nu)}{2(1-\nu)}\delta_n \tag{8}$$

where ν is the Poisson ratio and μ is the dynamic friction coefficient. Constants k_n, k_t, γ_n and γ_t are given by:

$$k_n = -\frac{4}{3}\sqrt{R^*}E^* \tag{9}$$

$$\gamma_n = -c_n\left(6m^*E^*\sqrt{R^*}\right)^{\frac{1}{2}} \tag{10}$$

$$k_t = -\mu_s\left[1-\left(1-\frac{\left\|\overrightarrow{\delta_t}\right\|}{\delta_{t,\max}}\right)^{\frac{3}{2}}\right]\frac{\left\|\overrightarrow{F_n^{el}}\right\|}{\left\|\overrightarrow{\delta_t}\right\|} \tag{11}$$

$$\gamma_t = -c_t\left(6\mu_s m^*\left\|\overrightarrow{F_n^{el}}\right\|\frac{\sqrt{1-\left\|\overrightarrow{\delta_t}\right\|/\delta_{t,\max}}}{\delta_{t,\max}}\right)^{\frac{1}{2}} \tag{12}$$

where, for a contact between particles i and j, R^* is the reduced radius $\left(\frac{1}{R^*} = \frac{1}{R_i} + \frac{1}{R_j}\right)$, E^* is the effective Young's modulus $\left(\frac{1}{E^*} = \frac{1}{E_i} + \frac{1}{E_j}\right)$, m^* is the geometric mean mass $\left(\frac{1}{m^*} = \frac{1}{m_i} + \frac{1}{m_j}\right)$, μ_s is the static friction coefficient, and c_n and c_t are the normal and tangential damping constants, respectively. The Coulomb criterion $\left\|\overrightarrow{F_t}\right\| \le \mu\left\|\overrightarrow{F_n}\right\|$ arises naturally as $\left\|\overrightarrow{\delta_t}\right\| \le \delta_{t,\max}$.

2.2 Simulation specifications

2.2.1 Particle properties

Two types of adsorbents are used to carry out this study: activated alumina and molecular sieve. They each represent a specific layer of adsorbent typically used in a TSA PPU. The ability of a DEM model to simulate a physical phenomenon relies mainly on the particle properties used in the contact force model. They need to be precisely measured or, at least, properly calibrated. The calibration

of a parameter must be done in such a way that the effect of this particular parameter is discriminated from the effect of the other parameters. In this study, the particle parameters are set using a mix of direct measurement and calibration methods. The particles density, Young's modulus and Poisson ratio presented in Table 1 were experimentally measured and incorporated directly into the DEM-based model.

Spherical particles were used to model the adsorbents since their sphericity is greater than 0.90. The particle porosity is 0.32–0.35 and 0.42–0.46 for the sieve and alumina particles, respectively. The Young's modulus is one of the most important parameters of a DEM model. If proper pressure measurements are to be obtained using the DEM, its value must be measured with great accuracy. The Young's modulus values were determined using a contact ultrasonic measurement method (Akseli and Cetinkaya 2008; Cetinkaya 2009; Li and Cetinkaya 2006). The Young's modulus determined for the activated alumina of the present study is consistent with that obtained for the similar alumina beads (catalyst support) using the single particle contact deformation method (Couroyer et al. 1999).

The specific particle size distribution (PSD) of each adsorbent is also integrated into the DEM-based model. Figure 1 displays the respective PSD.

The damping coefficients for the DEM-based model were calibrated using experimental measurements similar to the ones performed by Sondergaard et al. (1990). In these experiments, the coefficients of restitution (CoR) of each adsorbent type were measured following their impact on a horizontal steel plate after a free fall under gravity. Particles were dropped from a height of 208 mm as many times as needed to have 50 valid trials for each particle type. Since neither type of adsorbents is perfectly spherical, only the trials that resulted in a close to 90° rebound with respect to the surface were considered. Particle free falls were recorded by means of a high-speed camera at a frame rate of 120 fps. The normal CoR values of the alumina and molecular sieve adsorbents were measured at 0.68 ± 0.02 and 0.72 ± 0.01, respectively. The same free fall experiment was simulated using the DEM-based model with a varying normal damping factor (c_n) in order to obtain a calibration curve. Normal damping factors of 0.135 and 0.110 for the alumina and molecular sieve adsorbents best fitted the experimental CoR values. The same value of the normal damping factor was used for the particle–particle and particle–wall interactions. Also, like in previous work presented by Zhou et al. (1999) and Landry et al. (2004), it was assumed that the value of the tangential damping factor was the same as the normal one.

The friction coefficients for the DEM-based model were calibrated using experimental measurements of the angle of repose of a heap of particles. The same experiments as the ones described in Zhou et al. (2002) were carried out. The angles of repose were measured at $27.7° \pm 1.7°$ for the alumina particles and at $30.8° \pm 2.5°$ for the molecular sieve particles. After these trials, a complete numerical design of experiments (DOE) was performed to identify two friction factors (i.e. the particle–particle friction factor (μ_{pp}) and the particle–particle rolling friction factor $(\mu_{r,pp})$). It was found that, for both types of particles, $\mu_{pp} = 0.1335$ and $\mu_{r,pp} = 0.05$ provided the best fit with the

Table 1 Particle properties for the DEM-based model

Properties		Value	
		Alumina	Molecular sieve
Particle–particle interaction	Density $(\rho, kg/m^3)$	1,130	1,060
	Young's modulus (E, GPa)	9.02	3.57
	Poisson ratio (v)	0.2	0.3
	Normal damping coefficient $(c_{n,pp})$	0.135	0.110
	Tangential damping coefficient $(c_{t,pp})$	0.135	0.110
	Static friction coefficient $(\mu_{s,pp})$	0.1335	0.1335
	Dynamic friction coefficient (μ_{pp})	0.1335	0.1335
	Rolling friction coefficient $(\mu_{r,pp}, m)$	0.05	0.05
Particle–wall interaction	Normal damping coefficient $(c_{n,pw})$	0.135	0.110
	Tangential damping coefficient $(c_{n,pw})$	0.135	0.110
	Static friction coefficient $(\mu_{s,pw})$	0.2	0.2
	Dynamic friction coefficient (μ_{pw})	0.2	0.2
	Rolling friction coefficient $(\mu_{r,pw}, m)$	0.1	0.1

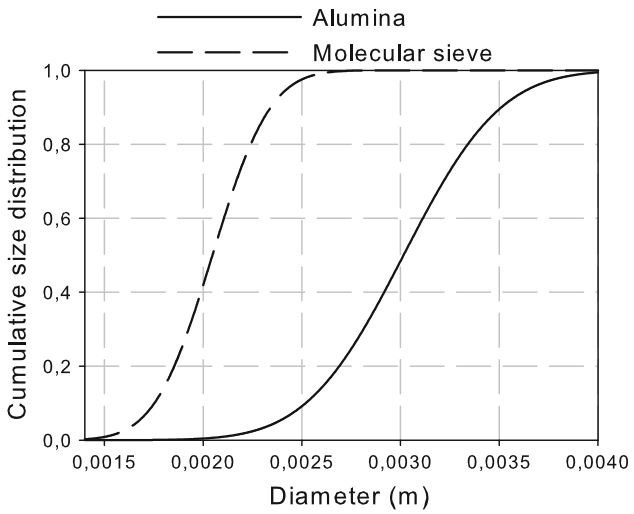

Fig. 1 Particle size distributions of the two adsorbents

experimental data. Simulated angles of repose of 27.0° and 28.4° were obtained for the alumina and molecular sieve particles, respectively. Following Zhou et al. (1999; 2001, 2002), the values of the corresponding particle–wall friction (μ_{pw}) and rolling friction $(\mu_{r,pw})$ coefficients were set to $\mu_{pw} = 1.5\mu_{pp}$ and $\mu_{r,pw} = 2\mu_{r,pp}$.

Table 1 presents a summary of the particle properties used in the DEM simulations.

2.2.2 Simulation time step

The value of the simulation time step should be a trade-off between numerical errors and stability, computational time and contact mechanics. Regarding the contact mechanics criterion, it was previously reported that, in the case of a model using non-linear springs (e.g. Hertzian dynamics), the critical time step (Δt_c) should be a fraction of the Rayleigh wave propagation time (Li et al. 2005). The Rayleigh time (t_R) is defined as (Johnson 1985):

$$t_R = \frac{\pi \overline{R}}{\beta}\sqrt{\frac{\rho}{G}} \tag{13}$$

where $\overline{R}$ is the mean particle radius and G the particle shear modulus given by:

$$G = \frac{E}{2(1+\nu)} \tag{14}$$

Finally, β is approximated by (Li et al. 2005):

$$\beta = 0.8766 + 0.163\nu \tag{15}$$

Li et al. (2005) and Gonzalez-Montellano et al. (2011) both used 20 % of the Rayleigh time as the simulation time step. Unfortunately, even the use of a fraction of the critical time step may sometimes yield numerically unstable results. In order to minimize the computational time, one must consider how the DEM software is programmed. In this study, a custom-made DEM program developed at Ecole Polytechnique de Montreal was used (Bertrand et al. 2005). This program is based on parallel programming and computing as well as other efficient data structures to reduce computational time significantly, especially when a large number of particles are simulated (Leclaire 2004). The fact that these data structures (e.g. list of neighboring particles) are shared by the processors (or cores) involved in a simulation and the use of an inappropriate time step may render a DEM simulation unstable. In particular, it was observed that updating these data structures at every N iterations, which entails the exchange of information between cores, may speed up the simulation significantly while preserving the accuracy of the solution. For this study, preliminary investigations revealed that the use of a 3.5×10^{-8} second time step with $N = 50$ required less computational time than the use of a 2.5×10^{-7} second time step, corresponding to $0.2t_R$, with an update of the data structures at every iteration $(N = 1)$. It should be noted that the DEM simulations performed for this study are extremely CPU intensive. It is also worth mentioning that it is common practice to use an abnormally low value of the Young's modulus in order to increase the time step (see Eq. 13) and reduce significantly the computational time (Gonzalez-Montellano et al. 2012b). This strategy is useful especially when only flow patterns are of interest. However, it cannot be applied here since studies of pressure measurements as well as particle dynamics are investigated.

2.2.3 Simulation domain

A schematic of the RFR is shown at Fig. 2. The air to be treated enters from the bottom of the unit and is fed to the radial packing through the annular channel during the adsorption phase and through the inner pipe during regeneration. In this configuration, the axial flow directions in the annular channel and in the inner pipe are the same. This configuration is identical to the "RZ arrangement" from Heggs et al. (1994) and the so-called "Cp z-flow" from Kareeri et al. (2006).

Because of the large amount of particles in the reactor, the value of the simulation time step and the computational resources available, a simulation of the whole reactor would be computationally out of reach. Therefore, a small volume element of this reactor, the shape of which represents a "wedge", such as the one identified in Fig. 2b, is used as the computational domain. The wedge is represented by a rectangle in the figure due to the large bed length to bed width ratio. Periodic boundary conditions are

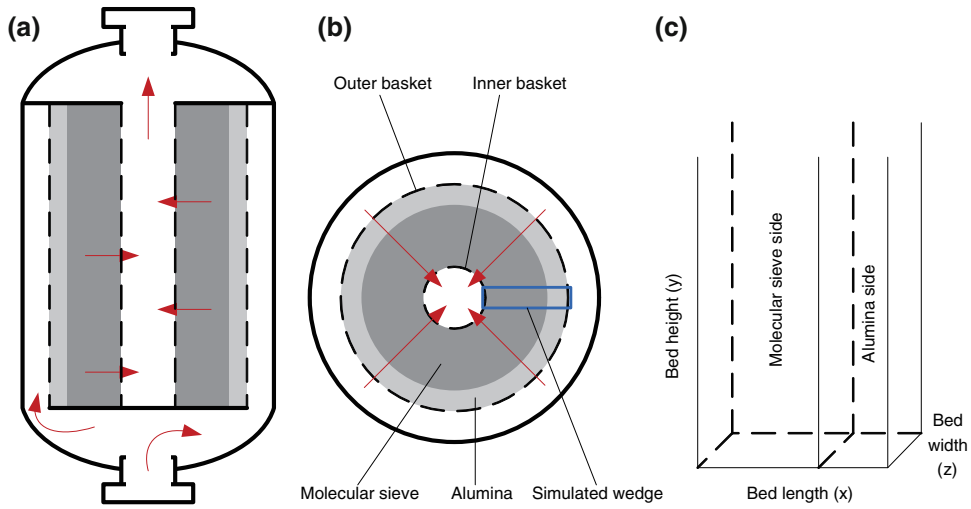

Fig. 2 Schematic of the RFR: **a** *front view*, **b** *top view* and **c** the DEM simulation domain

imposed on both sides along the width direction, which means that one particle flowing out of one side re-enters into the domain through the opposite side. It has been previously reported that the simulation domain size in the direction of the periodic boundary conditions should at least be five times the particle diameter in order to have no significant effect on the numerical results (Bertrand et al. 2004). Also, Landry et al. (2004) showed that a width of $2\overline{d}$ ($\overline{d}$ being the particles mean diameter) represents the transition from a 2D-like behavior to a 3D-like behavior. Here, the largest particle has a 4 mm diameter, so a 25 mm width is used. Such a scaled portion of the reactor is justified because it is axisymmetric and because of the occurrence of mainly radial dominated transfer mechanisms in the case of the radial expansion and contraction of the vessel.

To carry out this study, two computational domains are used. The specifications of each domain are presented in Table 2. The first computational domain (A) is used to calibrate and assess the DEM-based model. It serves to investigate the wall pressure evolution over the course of many wall motion cycles. For this part of the study, only alumina particles are considered since they are harder than the molecular sieve particles. For this domain, the height of the bed is emphasized and its length is compromised, which is justified by the fact that some relief in wall pressure is expected near the free surface. In other words, the use of a higher bed reduces the effect of the walls near the free surface. The second computational domain (B) contains both types of adsorbents and is used to study particle dynamics and mixing of the adsorbents at their interface (Fig. 2c). Here bed length is emphasized and the bed height is compromised because the length is the main direction along which mixing takes place when the walls are moved. The use of a shorter bed results in a larger effect of the free surface upon mixing, which can be viewed as a conservative strategy as less intense mixing is expected further away from the free surface. It should be noted that the top of the adsorbent bed is also a free surface in the full-scale unit. There is no horizontal plate at the top of the reactor and particles therein are free to move upward during wall motion.

The simulations of this work were done using a parallel implementation of the DEM based on the MPI library. All computations were performed using between 16 and 48 cores (Table 2) of the Compute Canada Mammouth supercomputer. The average computational time was in the order of 600 h for one second of simulated time.

2.2.4 *Reactor filling*

The computational domain is filled using a technique called "en masse" filling. With this technique, all particles are generated at the same time. They are loosely and evenly spread over the computational domain. They are then allowed to settle under gravity. Even though this technique is frequently used to save computational time (Gonzalez-Montellano et al. 2012b), it is used here for another important reason. During the filling process, the larger the

Table 2 Computational domain specifications

Domain	Dimensions (m)		Number of particles (Volume fraction)		Number of Cores
			Alumina	Molecular sieve	
A	Length	0.16	222,925 (1)	0 (0)	16
	Height	1.28			
	Width	0.025			
B	Length	0.32	51,467 (0.24)	547,513 (0.76)	48
	Height	0.64			
	Width	0.025			

height of the bed, the larger the velocities of the particles impacting its surface. These large particle velocities help to create a uniform tight packing, which is essential for a realistic simulation of the packed bed of a RFR. To fill two layers of particles in domain B, a zero thickness virtual wall is placed between the two types of adsorbents during the settling process. This wall is used to prevent any mixing of the adsorbents during the initial filling step. The two respective subdomains corresponding to each type of adsorbent are then clearly defined. Once the filling phase is complete, the virtual wall is removed and the particles are again allowed to settle in order to fill the voids that may have been created by the presence of this virtual wall.

2.2.5 *Wall motion cycle*

The DEM-based model is isothermal. The thermal expansion and contraction phenomena occurring in a TSA process are taken into account in the DEM-based model through the implementation of the corresponding wall motion. A typical temperature cycle of a full-scale unit TSA process is shown in Fig. 3a. Using the coefficient of thermal expansion of the materials used to build the RFR baskets, the corresponding radius change cycles for a full-scale unit are obtained (Fig. 3b).

TSA cycles usually last many hours (Ruthven 1984). The DEM simulation of such a long process is not feasible due to the small time step required. Some modifications must then be made to the original cycle so that it can be simulated using the DEM. It can be noticed that no temperature change occurs for approximately 50 % of the cycle. To save computational time, this portion of the cycle is removed for both baskets. To make sure that the particle dynamics is not affected significantly by this removal, a small portion of inactivity must be kept so that the energy gained during a cycle has time to dissipate before a new cycle begins. Figure 4 compares the original wall motion cycle and the one that was used for the DEM simulations. It must be mentioned that the radius change is not scaled down and corresponds to the wall motion occurring in the full-scale unit. Here again, such a strategy is deemed conservative as less mixing is then expected further away from the free surface.

Finally, a cycle frequency needs to be chosen for the simulations. Similar to the compromises made in the selection of the time step, the cycle frequency should be a trade-off between numerical stability, computational time and accurate prediction of the real TSA process. In fact, an adequate frequency is the one that allows the DEM-based model to simulate both dynamically and accurately a full-scale unit. Preliminary trial simulations revealed that it is

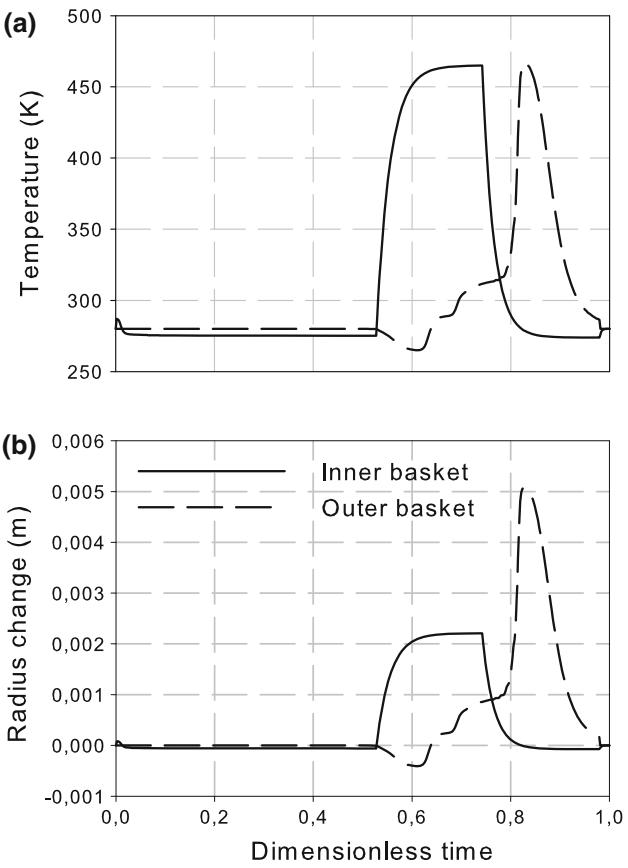

Fig. 3 Original temperature cycle (**a**) and corresponding radius change (**b**)

possible to identify an upper bound for the wall cycle frequency. In order for the simulation to be stable, it was found that the following criterion should hold:

$$\frac{\delta_{n,\max}}{V_{wall,\max}} > t_R \tag{16}$$

where t_R is defined in Eq. (13) and $\delta_{n,\max}$ is the normal overlap experienced by the smallest particle of the system following a normal impact with a wall velocity $V_{wall,\max}$, which corresponds to the maximum wall velocity attained for a specific wall cycle frequency. In other words, the characteristic impact time $\left(\frac{\delta_{n,\max}}{V_{wall,\max}}\right)$ inherent to the wall cycle frequency f should be higher than the characteristic time associated with the model (i.e. the Rayleigh wave propagation time t_R). The maximum wall velocity is linearly proportional to the wall cycle frequency:

$$V_{wall,\max} = kf \tag{17}$$

where k is a proportionality constant, which is equal to 24.5 m/cycle for the wall motion cycle displayed in Fig. 4. The stability criterion for the wall cycle frequency then becomes:

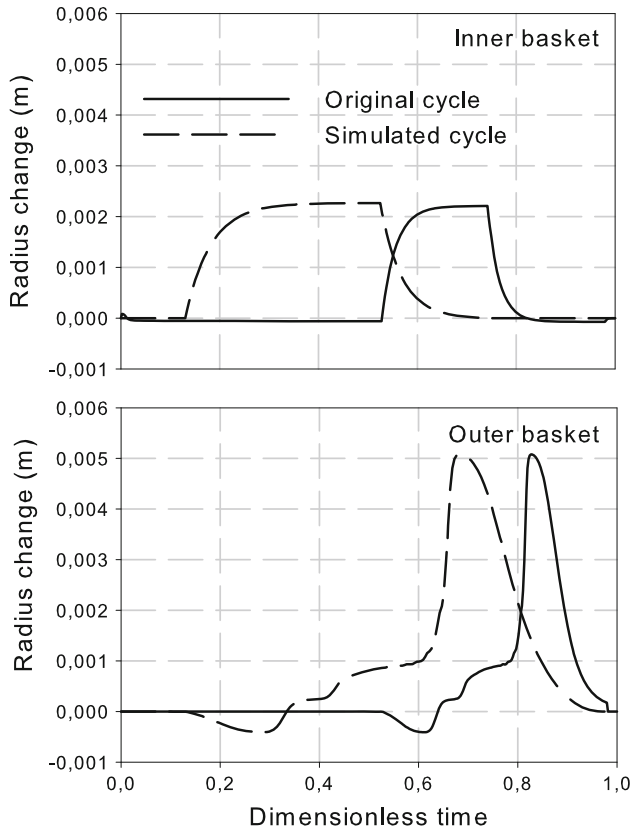

Fig. 4 Adapted wall motion cycle for the DEM simulations

$$\frac{\delta_{n,\max}}{kft_R} > 1 \tag{18}$$

Figure 5 shows the relationship between this criterion and the wall cycle frequency. It can readily be noticed that, in order for the simulation to be stable, the wall cycle frequency should be lower than 2 Hz. Frequencies of 0.5, 1 and 2 Hz were used for the DEM simulations of this work. The results are compared to experimental data measured on a full-scale unit in the next section.

3 Results and discussion

3.1 Model assessment

The DEM-based model is assessed by comparing bed porosity as well as static and dynamic wall pressures to both analytical and experimental results.

3.1.1 Bed porosity

If reliable numerical results are to be obtained from DEM simulations of a TSA process, the packed bed resulting from the filling process must have a porosity close to the one measured in a full-scale unit. RFR are filled using a

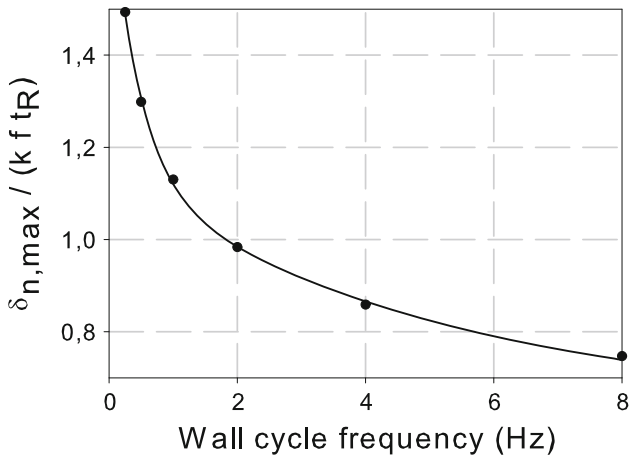

Fig. 5 Stability criterion versus wall cycle frequency

dense loading technique that generates a uniformly tight packed bed (Schneider et al. 1998). Kareeri et al. (2006) and Heggs et al. (1995a) respectively used bed porosity values of 0.3 and 0.4 to conduct their investigations. Most DEM studies have reported values varying between 0.38 and 0.42 after the filling process (Balevicius et al. 2011; Landry et al. 2003). Figure 6 displays bed porosities of the two computational domains after settling. A uniform porosity of 0.367 is observed for the alumina layer in both cases, and a value of 0.360 is obtained for the molecular sieve particles layer in computational domain B. The lower bed porosity obtained here can be attributed to the high polydispersity as well as the high impact velocities of the particles. Bed porosities of 0.35 for alumina and 0.34 for molecular sieve were measured experimentally. These differences between the DEM results and the experimental data are deemed reasonable.

3.1.2 Static stress analysis (no wall motion)

The wall pressure and shear stress computed by the DEM with no wall motion are compared to values predicted by Janssen's analysis. Janssen's analytical solution for wall normal pressure (σ_n) and wall shear stress (τ_w) is given by (Nedderman 2005):

$$\sigma_{xx} = \sigma_n = \frac{\gamma D_H}{4\mu_w}\left[1 - e^{\left(-\frac{4\mu_w K y}{D_H}\right)}\right] \tag{19}$$

$$\tau_w = \mu_w \sigma_n \tag{20}$$

where

$$\gamma = \rho_b g = \rho_p g(1-\varepsilon) \tag{21}$$

In these equations, γ is the weight of the granular material, ρ_b the bulk density, ρ_p the particle density, μ_w the friction coefficient between the bulk of particles and the

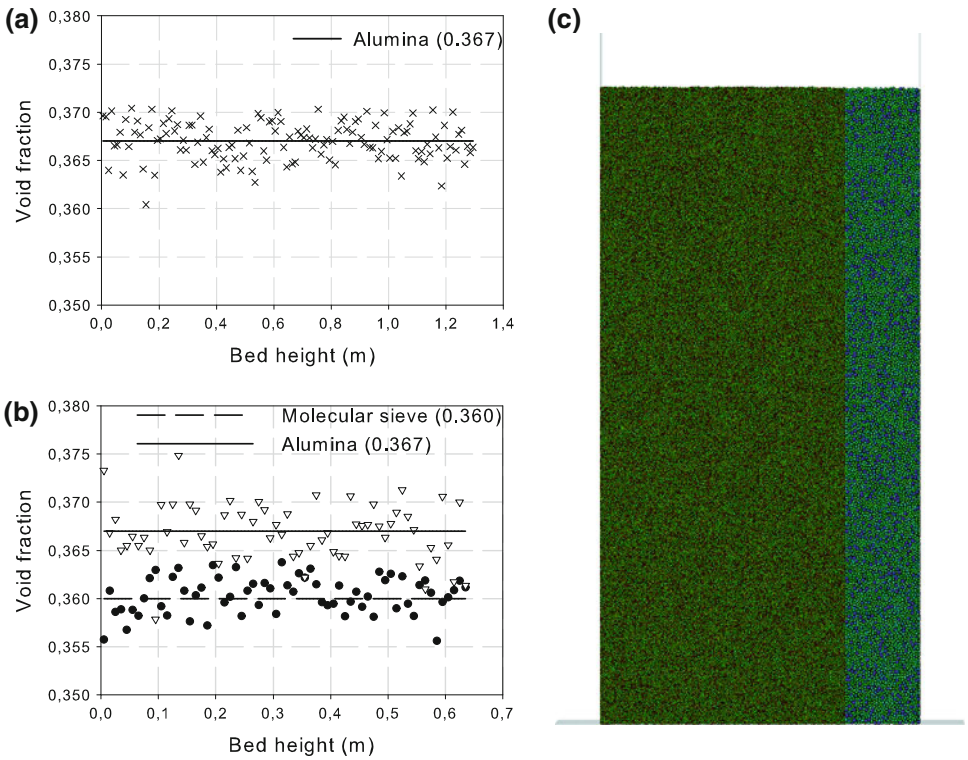

Fig. 6 Bed porosity with respect to bed height for **a** domain A, **b** domain B and **c** DEM packed bed after filling for domain B (particles are *colored* by size) (Color figure online)

wall, $K = \frac{1-\sin\phi}{1+\sin\phi}$ the Janssen constant and y the depth below the top surface of the bed. In this study, for comparison purposes, the internal friction angle ϕ is approximated using $\phi = \tan^{-1}\mu_{pp}$. The hydraulic diameter (D_H) is defined as:

$$D_H = \frac{4A}{P} \tag{22}$$

where A and P are respectively the cross-sectional area and the perimeter. It can be shown that, in the case of infinite parallel twin walls separated by a distance b, which applies to computational domains A and B, the hydraulic diameter is simply:

$$D_H = 2b \tag{23}$$

Note that Janssen's formulation for an annular bed is identical to the one presented here. Indeed, the hydraulic diameter of an annular bed with a distance b between the walls of two concentric cylinders is:

$$2b = (D_O - D_I) \tag{24}$$

where D_O and D_I are the external and internal diameters of the annular bed.

A comparison of the wall pressure and shear stress values from the DEM simulations and Janssen's Eqs. (19) and (20) using the particle properties of Table 1 are presented in Fig. 7. A quantitative match is obtained for the computational domain B while, for the taller computational domain A, an overshoot of the normal stress when the depth becomes twice as large as the bed hydraulic diameter is observed. This overshoot has been reported before in different circumstances (Balevicius et al. 2011; Landry et al. 2003). Two explanations for this overshoot in the case of the taller domain can be given.

The first possible explanation is related to the hypothesis made in Janssen's original analysis, which relies on three main assumptions: (a) the stresses are uniform across any horizontal section of the material, (b) the vertical and horizontal stresses are the dominant ones, and (c) the forces in play are at incipient failure on the basis of the Coulomb yield criterion (Landry et al. 2004; Nedderman 2005). The mobilized friction (μ_m), corresponding to the ratio of tangential forces to normal forces (Gonzalez-Montellano et al. 2012a), was computed to verify the last assumption. As can be seen in Fig. 8, the mobilized friction is always lower than the particle–wall friction $(\mu_{pw} = 0.2)$ used for the simulations. Just like in the work of Gonzalez-Montellano et al. (2012a) and Landry et al. (2004), a region at the top of the bed $(Y/D_H \to 0)$ having a significantly low μ_m is observed. It indicates that this region of the bed is far away from the Coulomb yield value; the walls support less stress so a hydrostatic stress profile is obtained. As for the rest of the bed, a mean value 0.16 is obtained for μ_m. This value is lower than μ_w (0.2), which partially explains why a larger hydrostatic region is predicted by the DEM. Gonzalez-Montellano et al. (2012b) studied in detail the effect of the

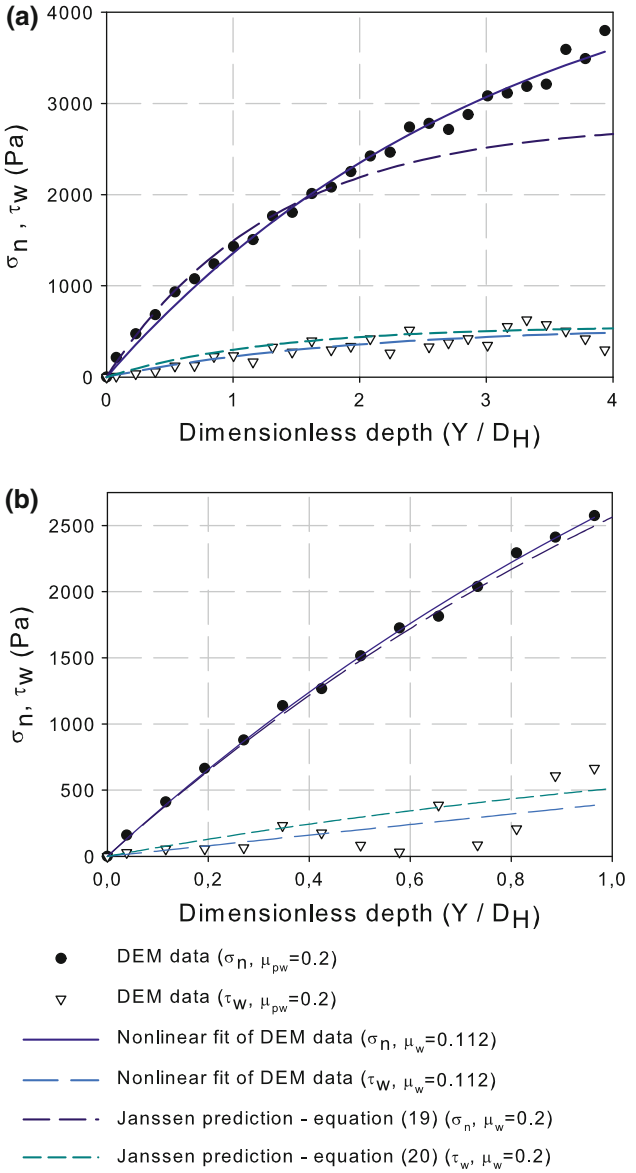

Fig. 7 Normal and shear stress values for computational domains **a** A and **b** B

"en masse" filling technique and concluded that this technique indeed reduces mobilization of friction. They specified that this filling technique could potentially lead to errors when predicting the wall pressures that develop during the filling of a silo. It must be noted that an incomplete development of friction is expected with the DEM since friction is mobilized by both the particle interactions and the particle shape (Hartl and Ooi 2008). In particular, the representation of the granular material by perfect spheres contributes to the decrease in friction mobilization. This means that the third assumption from Janssen's original analysis does not seem to apply in DEM simulations, which would explain the discrepancies between the numerical results and the analytical data. On the other hand, note that the depth-independent region of the normal stress profile, as obtained from Janssen's analysis, has still not been reached in the simulation. Consequently, it is possible that, with a taller bed, a quantitative agreement for the maximum normal stress would be obtained, like in Landry et al. (2003). Moreover, Fig. 7 shows that Janssen's equation best approximates the DEM data with a value of $\mu_w = 0.112$. This is lower than the value of μ_m, 0.16, obtained from Fig. 8 as discussed above. Therefore, this first explanation alone cannot elucidate completely why there is an overshoot in normal pressure in Fig. 7.

The second possible explanation is related to the parameters used in Eq. (19). The nonlinear fits displayed in Fig. 7 were obtained after applying a nonlinear least-square regression to determine values for coefficients μ_w and K. A quasi-identical value for K (0.71 instead of 0.76) and a much lower value for μ_w (0.112 instead of 0.2 (from Table 1)) are obtained. The coefficient μ_w used in Janssen's formulation should be the coefficient of friction between the bulk of particles and the wall (macroscopic friction) while the one used in the DEM-based model is the particle–wall interaction coefficient of friction (microscopic friction). Ketterhagen et al. (2009) presented a relationship between the macroscopic wall friction angle and the particle–wall friction coefficient for particles used in the simulation of a Schulze ring shear tester. This relationship indicates that, if the particles are allowed to rotate, the macroscopic friction can be significantly lower than the microscopic friction. Consequently, the lower values of the normal stress predicted by the Janssen's model could simply be explained by the inappropriate higher friction factor used in Eq. (19). To confirm this, three additional simulations were performed. They consist of varying the particle–wall friction coefficient (μ_{pw}) and filling domain A with a larger amount of particles (360,000), in order to

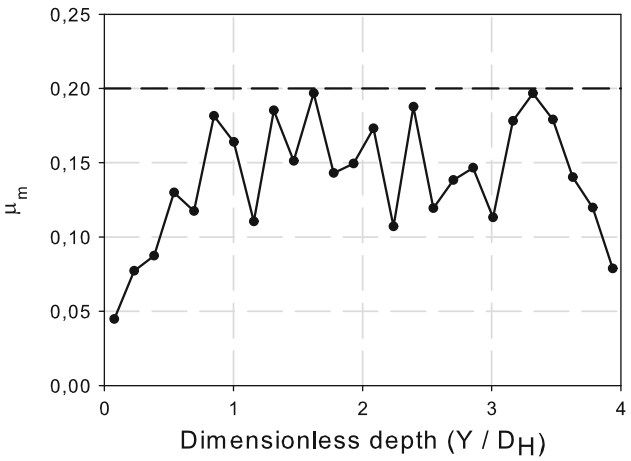

Fig. 8 Mobilized friction in computational domain A

have a taller bed and thus get closer to the asymptotic behavior and increase friction mobilization. Values of 0.1, 0.2 and 0.4 for μ_{pw} were tested. Figure 9 presents the wall pressure profiles obtained with the DEM-based model as well as the ones yielded by the Janssen's formulation when μ_{pw} is directly used in Eq. (19).

It can be observed that the agreement between the DEM results and Janssen's formulation is excellent when μ_{pw} is low, the discrepancies getting larger as μ_{pw} increases. Figure 10 shows the relationship between the macroscopic friction coefficient μ_w and the particle–wall friction coefficient μ_{pw} found by Ketterhagen et al. (2009) as well as the results obtained with the three DEM simulations. For the latter, the macroscopic friction coefficient μ_w corresponds to the value for which the DEM results best fit Janssen's formulation in Fig. 9. It can be noticed that the numerical results comply with those of Ketterhagen et al. (2009).

It must be recalled that, for the simulation of the shorter domain A, a value of $\mu_w = 0.112$ was found for $\mu_{pw} = 0.2$ (Fig. 7). This value of μ_w is well below the one found (0.166) with the taller bed (Fig. 10). This variation may indeed be attributed to the different bed heights used in the simulations of domain A. It also suggests that the two explanations proposed here for the overshoot in normal pressure (Fig. 7a) are plausible. Further investigation would be required to fully identify the sources of these discrepancies.

3.1.3 Dynamic stress analysis (with wall motion)

As was previously mentioned, a DEM simulation of the real experimental cycle, which is in the order of many hours, is not feasible. A much higher cycle frequency must then be chosen, which must however be such that the DEM-based model can yield numerical results that are phenomenologically accurate. One way to assess the reliability of the DEM-based model under dynamic conditions is to compare the numerical and experimental normal wall pressure values over the course of many cycles using the computational domain A. As already mentioned, the bed height is emphasized and the bed length is compromised in this computational domain, which is justified by the fact that some relief in wall pressure is expected near the free surface of the bed. The normal pressures for the full-scale unit and the DEM simulations are presented at Fig. 11. More precisely, experimental data for 10 cycles of the full-scale unit as well as 9, 7 and almost 4 cycles of DEM simulations with 2, 1 and 0.5 Hz cycle frequencies, respectively, are shown. Pressures in the full-scale unit were measured using load cells (Stellar Technology, Amherst, NY) mounted at various heights to the walls of both the inner and outer baskets. There was no significant

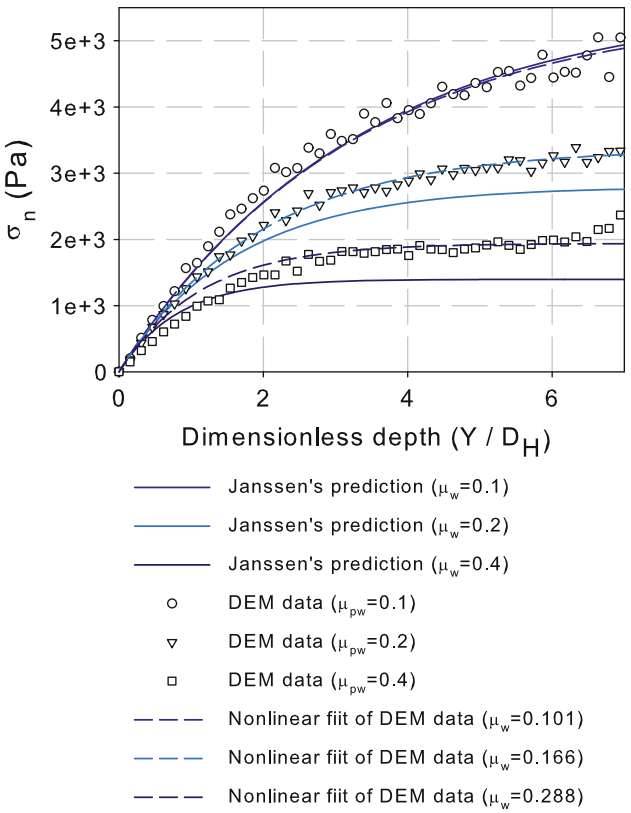

Fig. 9 Comparison of wall pressure for different values of the wall–particle friction coefficient

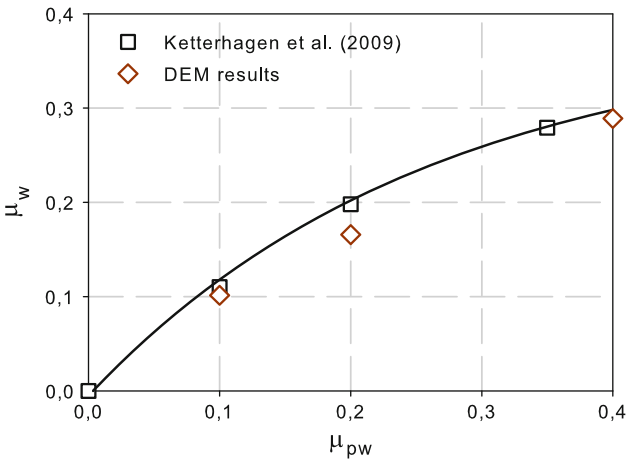

Fig. 10 Relationship between the macroscopic (μ_w) and microscopic friction (μ_{pw})coefficients

variation in wall pressure with respect to height for the number of cycles compared.

It can be readily noticed that a qualitative agreement between the numerical results and the experimental data is obtained. In all cycles, a maximum normal pressure peak is obtained followed by a drastic drop to zero. The pressure then levels off to an intermediate value before the beginning of the next cycle. Figure 12 displays the maximum

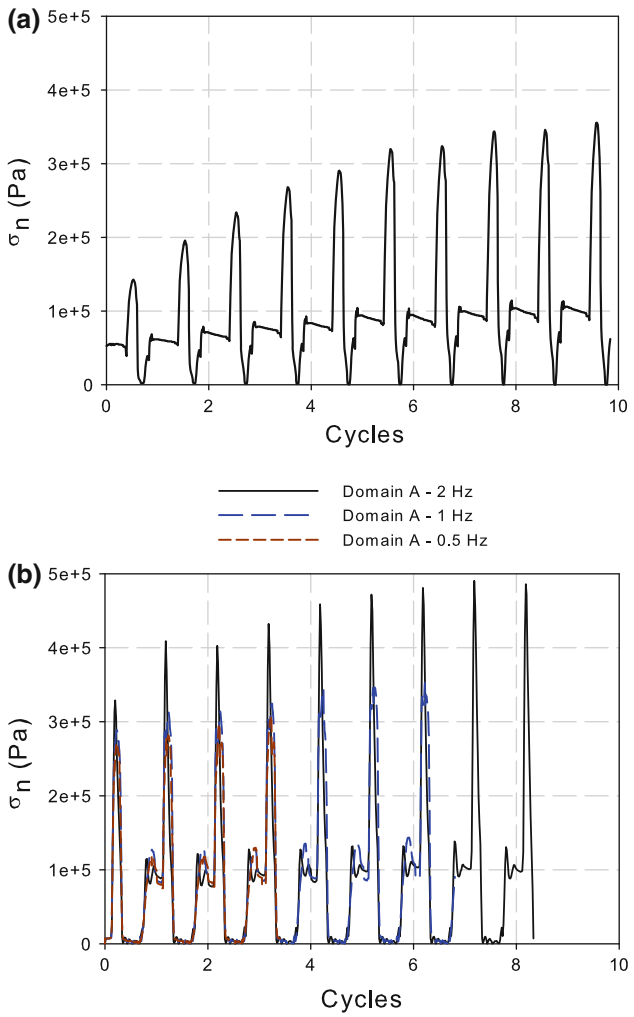

Fig. 11 Normal pressure evolution **a** for the full-scale unit and **b** the DEM simulations

pressure evolution in all cases and a progressive increase is observed. The increase is smoother with the DEM and a 0.5 or 1 Hz frequency than with both the DEM and a 2 Hz frequency and the full-scale unit. It can also be noticed that the curves corresponding to the DEM simulation with a 1 Hz cycle and the full-scale unit level off to similar values around 3.5×10^5 Pa. The simulation results with a 0.5 Hz frequency also indicate a similar trend after 4 cycles. On the other hand, the DEM simulation with a 2 Hz frequency overestimates the normal pressure measured in the full-scale unit after 9 cycles by more than 10 kPa. In fact, while the maximum pressure curve at this frequency follows a trend similar to the experimental curve, the results of Fig. 12 reveal that reducing the frequency from 2 to 1 and 0.5 Hz improves the asymptotic behavior significantly. As mentioned before, the wall cycle frequency should be strictly lower than 2 Hz. When analyzing the results of this figure, one should also keep in mind that the walls of the full-scale unit are elastic while the DEM-based model assumes rigid wall conditions. Note that the progressive increase in stress is a manifestation of thermal racking (Nedderman 2005). One observation here is that, by accounting for these thermal changes by means of radial expansion and contraction, the DEM is able to reproduce this phenomenon. To our knowledge, it is the first time that this phenomenon can be predicted using the DEM.

The accuracy of the DEM-based model cannot be assessed rigorously by comparing only the maximum value of the normal stress. Since particle dispersion is going to be evaluated below, the evolution of the numerical pressure with respect to the bed length should also match the one measured on the full-scale unit. The fact that the real reactor is much larger and the real cycle time is much longer does not allow a priori for a direct comparison. However, a closer look at the time variation of the compression/expansion speed of the granular bed for the full-scale unit and the DEM simulation reveals that it is possible to identify three similar characteristic phases within one single cycle. To identify these phases, the compression/expansion speed $\left(v_{c/e}\right)$ is introduced:

$$v_{c/e} = \frac{\Delta R_{t^*+\Delta t^*} - \Delta R_{t^*}}{\Delta t^*} \tag{25}$$

where ΔR is the bed length (i.e. the difference between the outer basket and inner basket positions) and t^* is the cycle time. A negative value of $v_{c/e}$ implies that the granular bed is being compressed while a positive value implies that it is expanding. These characteristic phases are clearly identified in Fig. 13. A detailed evolution of the normal pressure over the course of a single cycle (cycle 8 for the full-scale unit and cycle 6 for the DEM simulation with a 1 Hz frequency) is also presented in this figure.

At the end of the first compression phase, both bed lengths are reduced by approximately 2.5 mm (Fig. 13a, b). Since the bed is smaller than its initial length, a maximum pressure peak is expected in this phase. This can

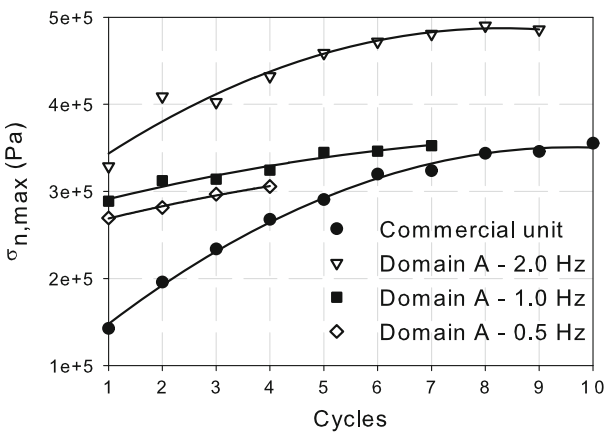

Fig. 12 Wall maximum pressure evolution

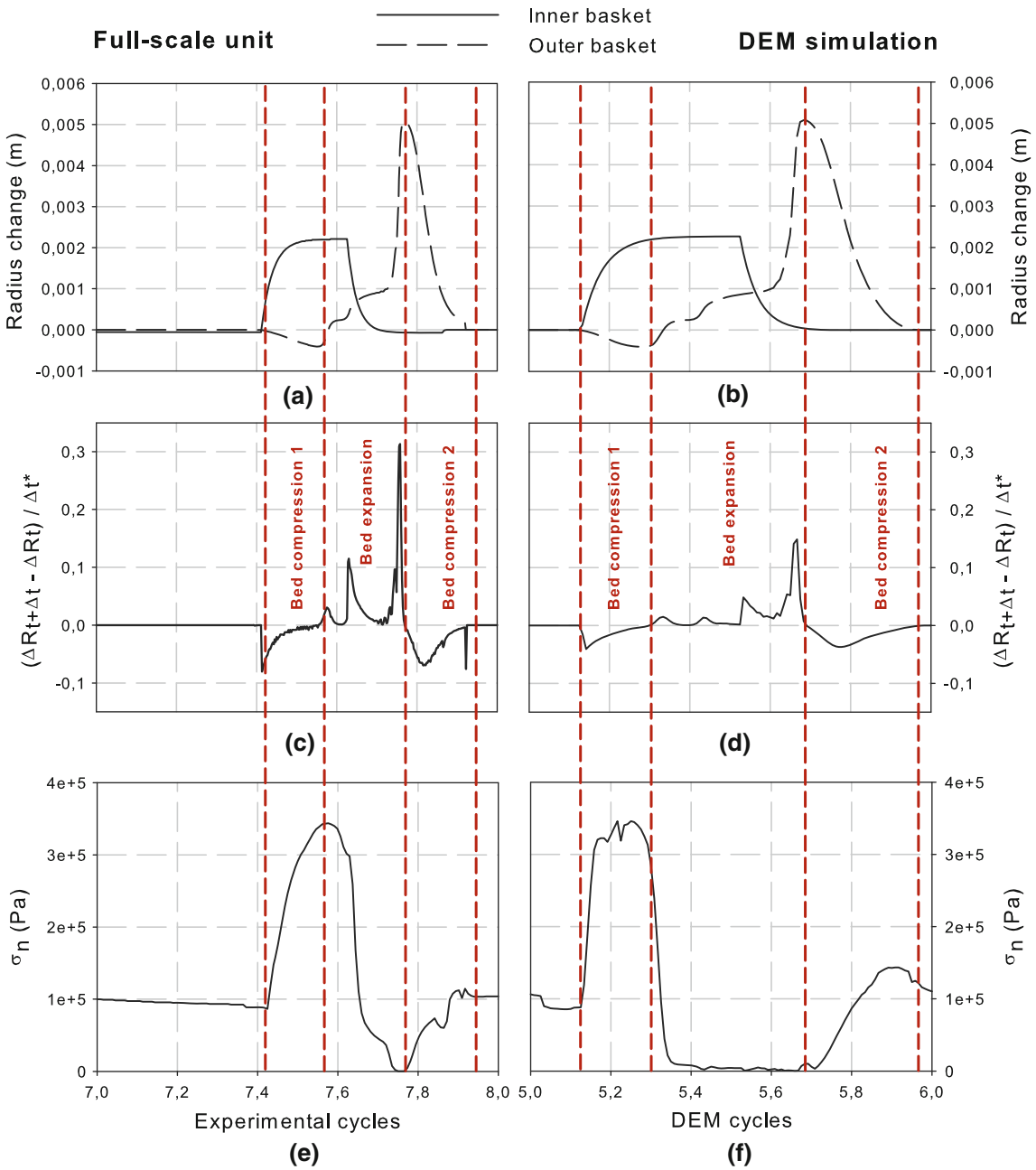

Fig. 13 Comparison over one single cycle of **a**–**c**–**e** experimental data and **b**–**d**–**f**) DEM simulation results: **a** and **b** radius change, **c** and **d** compression/expansion velocity and **e** and **f** normal pressure

indeed be seen in both the experimental and the numerical cases. However, the maximum pressure peak is obtained at the end of the first compression phase in the full-scale unit while it is obtained in the middle of this phase for the DEM simulation. Nevertheless, it can be noticed that the intensity of these peaks is similar.

At the end of the expansion phase, both beds are 5 mm longer than at the beginning of the cycle. It is expected that the normal pressure reaches zero in both cases. This is exactly what can be noticed in Fig. 13e and f. However, the decrease in pressure in the DEM simulation is faster and sharper than in the full-scale unit. Also, the time that the simulated pressure spent near the 0 Pa value is longer. This is due to the discrete nature of the wall motion. The first step of a DEM iteration consists of moving the walls. Then, the particle–particle and particle–wall contacts are detected and solved. The particles are moved by integrating Newton's second law only at the end of the iteration. So, if the bed is expanding, since the particles are not moved immediately, the number of contacts detected at the walls

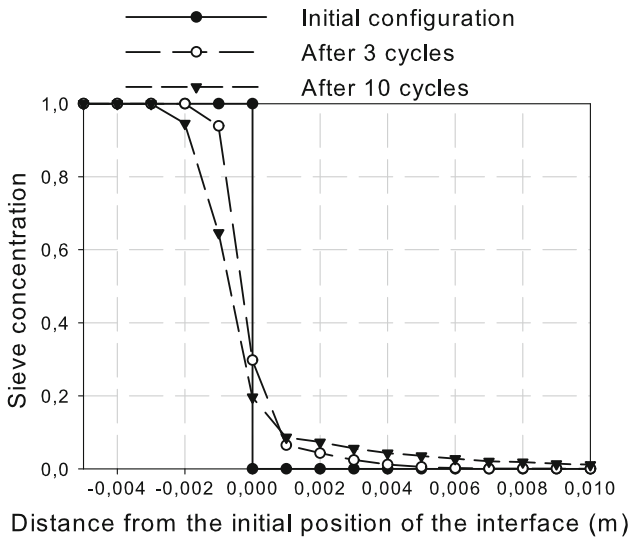

Fig. 14 Evolution of the molecular sieve surface concentration near the initial position of the interface

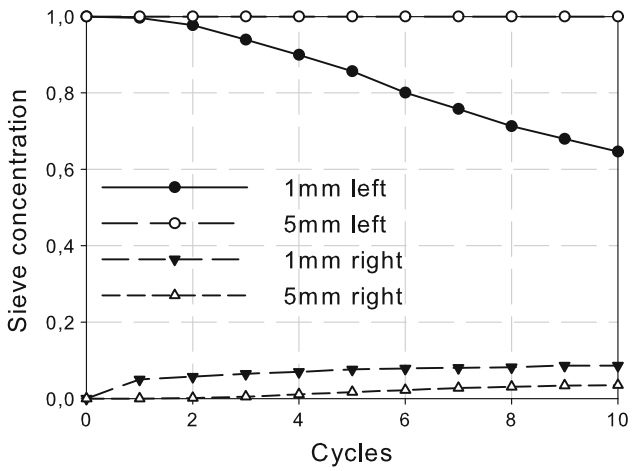

Fig. 15 Molecular sieve concentration on specific cross-section planes located at specific distance from the initial positioning of the interface

will diminish greatly and can even be zero. This explains the near-zero values of the wall pressure in the DEM simulation during the expansion phase.

In the last compression phase, both beds get compressed until their initial lengths are regained. For this reason, during this phase, the pressure is expected to steadily increase and level off to the value it had at the beginning of the cycle. It can be noticed in Fig. 13e and f that the pressure increase is slightly higher in the DEM simulation than in the full-scale unit, although, at the end of the cycle, a similar wall pressure is obtained in both cases.

In summary, good quantitative agreement between the experimental data and the numerical results was achieved in the different phases of the TSA cycle when a 1 Hz frequency is used for the simulation. These pressure results

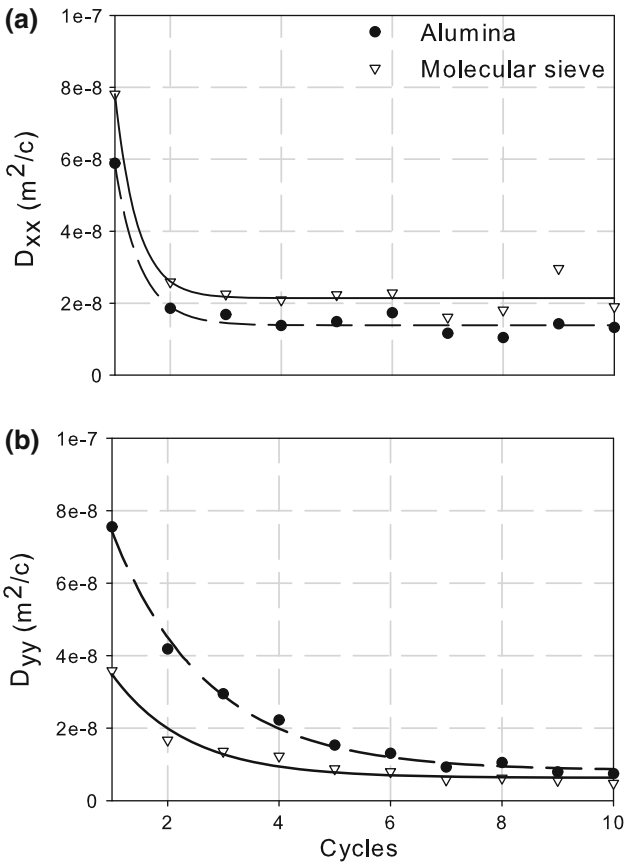

Fig. 16 **a** Radial (D_{xx}) and **b** axial (D_{yy}) dispersion coefficients

altogether show that the DEM-based model used in this work is accurate enough to predict the granular behavior in a RFR.

3.2 Investigation of particle dynamics

Particle dynamics and, in particular, mixing of the molecular sieve and alumina particles at their interface was simulated with the calibrated DEM-based model. The simulation domain B was considered for this part of the study. The goal was to derive a particle dispersion coefficient that could be used to predict the long-time mixing behavior of the particles. As already mentioned, the bed length is emphasized and the bed height is compromised in this computational domain because the bed length is the main direction along which mixing takes place when the walls are moved. The domain walls were moved with a 1 Hz frequency. Figure 14 displays the evolution of the "surface" concentration of molecular sieve particles for 10 cycles near the initial position of the interface. It represents the fraction of molecular sieve particles (the surface occupied by the molecular sieve particles divided by the surface occupied by all the particles) on a cross-section plane covering the entire domain height. This figure clearly

shows that the concentration of molecular sieve particles left of the initial position of the interface decreases with time, which indicates that alumina particles are migrating into this region. Quite obviously, a similar phenomenon occurs right of this interface, where the concentration of alumina particles diminishes with time owing to the migration of molecular sieve particles into this region.

The evolution of the molecular sieve concentration over the course of 10 cycles on cross-section planes on both side of the initial interface and that are 1 and 5 mm away from it are presented in Fig. 15. It can be noticed that the decrease in sieve concentration 1 mm left of the interface is sharper than the increase 1 mm right this interface. This is explained by the smaller average size of the molecular sieve particles. Also, no change in the molecular sieve concentration 5 mm left of the interface can be observed while some changes are noticeable 5 mm right of this interface. Again, this is a direct consequence of the size differences between the two particle types. Since the bed of particles is slightly denser on the molecular sieve side and since the alumina particles are bigger on average than the molecular sieve ones, these alumina particles are expected to be hampered and slowed down significantly. Nevertheless, some particle migration is observed.

To quantify the extent of the particle migration, a dispersion coefficient (Einstein 1905) was computed as:

$$D_{xx} = \frac{\sigma_x^2}{2t} = \frac{\sum_{i=1}^{N} (\Delta x_i - \Delta\bar{x})^2}{2(N-1)t} \tag{26}$$

In this expression, t stands for the time in cycle units, Δx is the particle displacement along the radial direction (perpendicular to the interface), $\Delta\bar{x}$ the mean particle displacement and N the number of particles in a rectangular box circumscribing the interface. Figure 16a shows that the dispersion coefficients in the x-direction for both particle types decrease rather rapidly initially, but then level off to values around 1×10^{-8} m^2/cycle for the alumina particles and 2×10^{-8} m^2/cycle for the molecular sieve particles. The difference between the two coefficients is likely due to the fact that the alumina particles are larger than the molecular sieve particles, thereby reducing their mobility near the interface. The higher value of the dispersion coefficients observed in the first few cycles can be attributed to the free space at the interface, which is due to the removal of the invisible wall used during the filling process to prevent the two types of particles from mixing. The dispersion coefficients in the y-direction (Fig. 16b) exhibit the same behaviour as in the x-direction except that they level off to the same value (1×10^{-8} m^2/cycle). It must be noted that, since the motion of the simulated walls is more intense than that in the full-scale unit because of the differences in the temperature cycles, the computed dispersion coefficients represent an upper bound.

These dispersion coefficients could be used in a transient diffusion equation to predict the extent of mixing occurring at the interface of a full-scale size RFR. It is known that particle mixing can have a significant deteriorative effect on the reactor efficiency. In this way, the dispersion coefficients could also be used to set an upper limit for the bed operation lifetime. Nevertheless, the results obtained here indicate that particle motion across the interface is relatively slow.

4 Conclusion

A DEM-based model was successfully applied to study the dynamics of adsorbents used in the RFR of a TSA process. The thermal swing cycle was simulated by a corresponding wall motion cycle in the DEM. It was shown that, if the model is properly calibrated using a mix of direct measurements of particle properties and simple auxiliary simulations, it can predict phenomenologically the granular flow behavior in a full-scale unit. The accuracy of the DEM-based model was assessed using experimental values of bed porosity, analytical values of predicted wall pressure based on Janssen's theory, and experimental values of wall pressure measured during the operation of a full-scale unit. Qualitatively and quantitatively good agreement was obtained for porosity as well as static (i.e. with no wall motion) and dynamic (i.e. with wall motion) wall pressure. It was noticed that, in the case of a tall computational domain, the DEM yielded wall pressure values that exceed the values predicted by Janssen's analysis. Further investigation would be required to clearly identify the cause of this discrepancy. Moreover, the dynamic pressure obtained by the DEM simulation was observed to comply well with every phase of a full-scale unit cycle. The DEM-based model was also able to reproduce the thermal racking phenomenon occurring is this type of reactor. Finally, the dispersion of particles during many wall motion cycles was investigated using the simulation of a packed bed containing layers of alumina and molecular sieve particles. While the corresponding dispersion coefficients indicate that little mixing occurs at the adsorbent interface, they show that mixing could potentially affect the efficiency of the reactor in the long run.

To our knowledge, this is the first time that simulation is used to investigate the behavior of the packed bed of a RFR in a TSA process. The results obtained with the proposed model show that the DEM is a valuable tool for the investigation of such slow dynamical processes, provided a careful calibration is done.

Acknowledgments The financial support of the Natural Sciences and Engineering Research Council of Canada (NSERC) and PRAXAIR Inc. is gratefully acknowledged. All simulations were made possible thanks to the computational resources of Compute Canada.

References

Ackley, M.W., Celik, C.E., Nowobilski, J.J., Schneider, J.S.: Radial flow reactor. US 8,101,133 B2, 24 Jan (2012)

Akseli, I., Cetinkaya, C.: Drug tablet thickness estimations using air-coupled acoustics. Int. J. Pharm. **351**(1–2), 165–173 (2008)

Balevicius, R., Sielamowicz, I., Mroz, Z., Kacianauskas, R.: Investigation of wall stress and outflow rate in a flat-bottomed bin: a comparison of the DEM model results with the experimental measurements. Powder Technol. **214**(3), 322–336 (2011)

Bertrand, F., Gange, T., Desaulniers, E., Vidal, D., Hayes, R.E.: Simulation of the consolidation of paper coating structures: probabilistic versus deterministic models. Comput. Chem. Eng. **28**(12), 2595–2604 (2004)

Bertrand, F., Leclaire, L.A., Levecque, G.: DEM-based models for the mixing of granular materials. Chem. Eng. Sci. **60**, 2517–2531 (2005)

Celik, C.E., Ackley, M.W.: Radial bed vessels having uniform flow distribution. US 8,313,561 B2, 20 Nov (2012)

Cetinkaya, C.: Accoustic Measurement of Young's Modulus and Poisson's Ratio for Adsorbents Beads. In: unpublished Praxair Project Progress Report (375–35322), Clarkson University. (2009)

Couroyer, C., Ning, Z., Ghadiri, M., Brunard, N., Kolenda, F., Bortzmeyer, D., Laval, P.: Breakage of macroporous alumina beads under compressive loading: simulation and experimental validation. Powder Technol. **105**, 57–65 (1999)

Cundall, P.A., Strack, O.D.L.: Discrete numerical model for granular assemblies. Geotechnique **29**(1), 47–65 (1979)

Einstein, A.: Motion of suspended particles on the kinetic theory. Ann. Phys. **17**(3), 549–560 (1905)

Fraige, F.Y., Langston, P.A.: Integration schemes and damping algorithms in distinct element models. Adv. Powder Technol. **15**(2), 227–245 (2004)

Goda, T.J., Ebert, F.: Three-dimensional discrete element simulations in hoppers and silos. Powder Technol. **158**(1–3), 58–68 (2005)

Gonzalez-Montellano, C., Gallego, E., Ramirez-Gomez, A., Ayuga, F.: Three dimensional discrete element models for simulating the filling and emptying of silos: analysis of numerical results. Comput. Chem. Eng. **40**, 22–32 (2012a)

Gonzalez-Montellano, C., Ramirez, A., Fuentes, J.M., Ayuga, F.: Numerical effects derived from en masse filling of agricultural silos in DEM simulations. Comput. Electron. Agric. **81**, 113–123 (2012b)

Gonzalez-Montellano, C., Ramirez, A., Gallego, E., Ayuga, F.: Validation and experimental calibration of 3D discrete element models for the simulation of the discharge flow in silos. Chem. Eng. Sci. **66**(21), 5116–5126 (2011)

Hartl, J., Ooi, J.Y.: Experiments and simulations of direct shear tests: porosity, contact friction and bulk friction. Granul. Matter **10**(4), 263–271 (2008)

Heggs, P.J., Ellis, D.I., Ismail, M.S.: Modelling of fluid-flow distributions in annular packed beds. Gas Sep. Purif. **8**(4), 257–264 (1994)

Heggs, P.J., Ellis, D.I., Ismail, M.S.: Evaluation of pressure profiles and overall pressure drop for flow through annular packed bed configurations. Gas Sep. Purif. **9**(3), 171 (1995a)

Heggs, P.J., Ellis, D.I., Ismail, M.S.: Prediction of flow distributions and pressure changes in multi-layered annular packed beds. Gas Sep. Purif. **9**(4), 243 (1995b)

Hidano, T., Nakamura, M., Kawai, M.: Pre-purification unit of cryogenic air separation unit, hydrocarbon adsorbent, and method of pre-treating feed air. US 7,931,736 B2, 26 Apr (2011)

Johnson, K.L.: Contact Mechanics. Cambridge University Press, Cambridge (1985)

Kalbassi, M.A., Golden, T.C.: Purification of gases using solid adsorbents. US 5,855,650, 5 Jan (1999)

Kareeri, A.A., Zughbi, H.D., Al-Ali, H.H.: Simulation of flow distribution in radial flow reactors. Ind. Eng. Chem. Res. **45**, 2862–2874 (2006)

Ketterhagen, W.R., Curtis, J.S., Wassgren, C.R., Hancock, B.C.: Predicting the flow mode from hoppers using the discrete element method. Powder Technol. **195**(1), 1–10 (2009)

Ko, D., Kim, M., Moon, I., Choi, D.: Analysis of purge gas temperature in cyclic TSA process. Chem. Eng. Sci. **57**(1), 179–195 (2002)

Kumar, R., Deng, S.: Trace carbon monoxide and hydrogen conversion prior to cryogenic distillation of air. Adsorption **12**(5–6), 361–373 (2006)

Kumar, R., Dissinger, G.R.: Nonequilibrium, nonisothermal desorption of single adsorbate by purge. Ind. Eng. Chem. Process Des. Dev. **25**(2), 456–464 (1986)

Kumar, R., Huggahalli, M., Bülow, M.: Thermal swing adsorption process. US 6,432,171 B1, 13 Aug (2002)

Landry, J.W., Grest, G.S., Plimpton, S.J.: Discrete element simulations of stress distributions in silos: crossover from two to three dimensions. Powder Technol. **139**(3), 233–239 (2004)

Landry, J.W., Grest, G.S., Silbert, L.E., Plimpton, S.J.: Confined granular packings: structure, stress, and forces. Phys. Rev. E (Stat. Nonlinear Soft Matter Phys. **67**(4), 41301–41303 (2003)

Leclaire, L.-A.: Parallélisation de la méthode des éléments discrets appliquée aux écoulements granulaires (Parallelization of the discrete element method applied to granular flows). Mémoire de maîtrise (Ecole polytechnique de Montréal) (2004)

Lemieux, M., Bertrand, F., Chaouki, J., Gosselin, P.: Comparative study of the mixing of free-flowing particles in a V-blender and a bin-blender. Chem. Eng. Sci. **62**(6), 1783–1802 (2007)

Li, C., Cetinkaya, C.: Frequency domain thickness measurement approach for microscale multilayered structures. IEEE Trans. Instrum. Meas. **55**(1), 206–211 (2006)

Li, Y., Xu, Y., Thornton, C.: A comparison of discrete element simulations and experiments for 'sandpiles' composed of spherical particles. Powder Technol. **160**(3), 219–228 (2005)

Libal, K., Fierlbeck, W., Von Gemmingen, U.: Adsorption reactor solid cage walls—for minimal erosion of contained solids during adaptation to temp. Change by inherent expansion of the walls. US 5,827,485, 27 Oct (1998)

Lobanov, E.L., Skipin, Y.A.: Increasing the operating efficiency of radial reactors in reforming. Chem. Technol. Fuels Oils **22**(5–6), 275–278 (1986)

Masson, S., Martinez, J.: Effect of particle mechanical properties on silo flow and stresses from distinct element simulations. Powder Technol. **109**(1–3), 164–178 (2000)

Nedderman, R.M.: Statics and Kinematics of Granular Materials, Digitally printed 1st pbk edn. Cambridge University Press, Cambridge (2005)

Ponzi, P.R., Kaye, L.A.: Effect of flow maldistribution on conversion and selectivity in radial flow fixed-bed reactors. AIChE J. **25**(1), 100–108 (1979)

Rapaport, D.C.: Radial and axial segregation of granular matter in a rotating cylinder: a simulation study. Phys. Rev. E (Stat. Nonlinear Soft Matter Phys.) **75**(3), 31301 (2007)

Ruthven, D.M.: Principles of Adsorption and Adsorption Processes. Wiley, New York (1984)

Schneider, J.S., Smolarek, J., Ackley, M.W., Nowobilski, J.J.: Assembly and method for loading particles into a vessel. US 5,836,362-A, 17 Nov (1998)

Seader, J.D., Henley, E.J.: Separation Process Principles. Wiley, New York (1998)

Sondergaard, R., Chaney, K., Brennen, C.E.: Measurements of solid spheres bouncing off flat plates. J. Appl. Mech. Trans. ASME **57**(3), 694–699 (1990)

Sudah, O.S., Arratia, P.E., Alexander, A., Muzzio, F.J.: Simulation and experiments of mixing and segregation in a tote blender. AIChE J. **51**(3), 836–844 (2005)

Tsuji, Y., Tanaka, T., Ishida, T.: Lagrangian numerical simulation of plug flow of cohesionless particles in a horizontal pipe. Powder Technol. **71**(3), 239–250 (1992)

Zhou, Y.C., Wright, B.D., Yang, R.Y., Xu, B.H., Yu, A.B.: Rolling friction in the dynamic simulation of sandpile formation. Phys. A **269**(2), 536–553 (1999)

Zhou, Y.C., Xu, B.H., Yu, A.B., Zulli, P.: Numerical investigation of the angle of repose of monosized spheres. Phys. Rev. E (Stat. Nonlinear Soft Matter Phys.) **64**(2 I), 213011–213018 (2001)

Zhou, Y.C., Xu, B.H., Yu, A.B., Zulli, P.: An experimental and numerical study of the angle of repose of coarse spheres. Powder Technol. **125**(1), 45–54 (2002)